

Universality of scanning tunneling microscopy in cuprate superconductorsPeayush Choubey,^{1,2} Andreas Kreisel,^{3,4} T. Berlijn,⁵ Brian M. Andersen,⁴ and P. J. Hirschfeld¹¹*Department of Physics, University of Florida, Gainesville, Florida 32611, USA*²*Department of Physics, Indian Institute of Science, Bengaluru 560012, India*³*Institut für Theoretische Physik, Universität Leipzig, D-04103 Leipzig, Germany*⁴*Niels Bohr Institute, Juliane Maries Vej 30, University of Copenhagen, DK-2100 Copenhagen, Denmark*⁵*Center for Nanophase Materials Sciences and Computational Sciences and Engineering Division, Oak Ridge National Laboratory, Oak Ridge, Tennessee 37831, USA*

(Received 30 June 2017; revised manuscript received 19 October 2017; published 28 November 2017)

We consider the problem of local tunneling into cuprate superconductors, combining model-based calculations for the superconducting order parameter with wave function information obtained from first-principles electronic structure. For some time it has been proposed that scanning tunneling microscopy (STM) spectra do not reflect the properties of the superconducting layer in the CuO_2 plane directly beneath the STM tip, but rather a weighted sum of spatially proximate states determined by the details of the tunneling process. These “filter” ideas have been countered with the argument that similar conductance patterns have been seen around impurities and charge ordered states in systems with atomically quite different barrier layers. Here we use a recently developed Wannier function-based method to calculate topographies, spectra, conductance maps, and normalized conductance maps close to impurities. We find that it is the local planar Cu $d_{x^2-y^2}$ Wannier function, qualitatively similar for many systems, that controls the form of the tunneling spectrum and the spatial patterns near perturbations. We explain how, despite the fact that STM observables depend on the materials-specific details of the tunneling process and setup parameters, there is an overall universality in the qualitative features of conductance spectra. In particular, we discuss why STM results on $\text{Bi}_2\text{Sr}_2\text{CaCu}_2\text{O}_8$ (BSCCO) and $\text{Ca}_{2-x}\text{Na}_x\text{CuO}_2\text{Cl}_2$ (NaCCOC) are essentially identical.

DOI: [10.1103/PhysRevB.96.174523](https://doi.org/10.1103/PhysRevB.96.174523)**I. INTRODUCTION**

Scanning tunneling microscopy (STM) and spectroscopy (STS) have played an important role in the evolution of ideas about cuprate superconductors, including the d -wave symmetry of the superconductivity, the nature of the pseudogap, and the existence of competing orders [1,2]. On the other hand, exactly what is measured by STM and STS has never been completely clear, due to the fact that the superconducting wave function is believed to reside primarily in the CuO_2 layer, while the STM tip detects a tunneling current ascribed to the density of electronic states several Å above the cleaved surface. Between the two lie insulating barrier layers that are different for each cuprate material. For example, in the canonical STM material $\text{Bi}_2\text{Sr}_2\text{CaCu}_2\text{O}_8$ (BSCCO), the insulating layer consists of BiO and SrO planes, with the latter containing a so-called apical O atom placed directly above a Cu in the CuO_2 plane below the BiO layer at which the system cleaves. In another intensively studied material, $\text{Ca}_{2-x}\text{Na}_x\text{CuO}_2\text{Cl}_2$ (NaCCOC), the barrier layer contains planes of Cl and planes of Ca/Na atoms, with no apical O, see Figs. 1(a) and 1(b). Instead, NaCCOC contains apical Cl, which resides on the surface of the cleaved layer. If the tunneling process depends on the details of the barrier layer, one might expect to see very different results for different cuprate materials, even if their superconducting states are quite similar. In practice, most theoretical work has ignored this complication and assumed a featureless barrier.

To reveal the effects of the barrier layer most clearly, a homogeneous situation is not ideal, since the range of the tunneling process is hidden by the crystal periodicity [3]. On the other hand, studies of impurity effects in superconductors

have been shown to be very useful in elucidating aspects of the superconductivity [4,5]. In cuprates, Zn and Ni impurities have been widely studied as they substitute an in-plane Cu atom and hence directly couple to the electronic states that give rise to the superconducting properties. With a closed d shell, Zn acts as a strong nonmagnetic potential scatterer, whereas Ni acts as a magnetic scatterer owing to its $3d^8$ configuration. The STM tunneling conductance around Zn in BSCCO features a sharp in-gap virtual bound state and drastic suppression of the coherence peaks [6], consistent with the simplest theoretical predictions for a nonmagnetic δ -function potential [7] in a d -wave superconductor. However, the spatial pattern around the impurity site deviates from the predictions of this simple model [4]. Most notably, experiment observes intensity maxima at the impurity sites in contrast to the minima predicted by the theory.

To reconcile theory and experiment, several authors focused on the details of the tunneling process, and advanced a hypothesis that we will refer to as a “filter”; in essence, these works proposed phenomenologically that the tip detected the signal arising from the four nearest-neighbor (NN) Cu sites, rather than from that immediately below the tip [8,9]. The authors of Ref. [8] suggested, in particular, that the overlap of the apical oxygen $2p_z$ and $3s$ orbitals with Bi p_z was crucial for the tunneling. While a first-principles calculation of a Zn impurity in BSCCO detected a weak filter effect [10], the effect of superconductivity was unknown. More recently, a hybrid theory was proposed [11,12] that accounted for material-specific details by down-folding density functional theory calculations onto a tight-binding model using Cu $3d_{x^2-y^2}$ Wannier functions, and combined this with a phenomenological Bogoliubov-de Gennes (BdG) calculation of d -wave superconductivity in this basis. This BdG+W theory was able

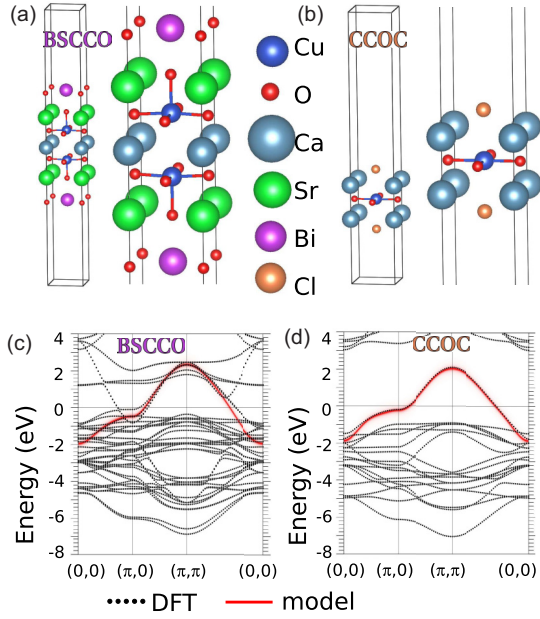


FIG. 1. Crystal structure of (a) $\text{Bi}_2\text{Sr}_2\text{CaCu}_2\text{O}_8$ and (b) $\text{Ca}_2\text{CuO}_2\text{Cl}_2$ surface as used for the DFT calculation. Band structure (black dots) of (c) $\text{Bi}_2\text{Sr}_2\text{CaCu}_2\text{O}_8$ and (d) $\text{Ca}_2\text{CuO}_2\text{Cl}_2$ surface compared to down-folding to a one-band model (red solid line).

to account for the details of the Zn resonance in BSCCO and many aspects of the quasiparticle interference data on this material [12]. Furthermore, using a variant of the same method applicable to t - J -type models, it was recently shown [13] that the characteristics of d form factor charge order, where charge modulations occur mainly at O sites and are opposite in phase for two inequivalent O atoms [14–16], can be easily obtained within a one-band calculation by accounting for the O degrees of freedom through the Wannier function.

Nevertheless, while this model successfully accounted for STM data on Zn impurities in BSCCO as well as quasiparticle interference results in exquisite detail, it confirmed that the wave functions at the surface detected by the tip were influenced strongly by their hybridization with the apical oxygen $2p_z$ states. As discussed above, these apical O states are present in most cuprates, but not in NaCCOC. The previous Wannier-based work thus fails to address the question of the apparent universality of STM observables, e.g., impurity states and charge order, in different cuprate materials [17]. In this paper, we attempt to reconcile the filter proposals with the universality of STM response observed in cuprates.

For this purpose, we apply the BdG+W approach to the impurity problem in both BSCCO and NaCCOC. We review the BSCCO Zn results, and move on to discuss the Ni impurity results from BSCCO, which were not addressed in Ref. [12]. STM studies on BSCCO [18] have shown two spin-resolved in-gap virtual bound states at energies $\pm\Omega_{1,2}^{\text{expt}}$. Bound state peaks were observed to be particlelike at the impurity site and next-nearest-neighbor (NNN) sites, and holelike at the nearest-neighbor sites. The spatial patterns at $+\Omega_{1,2}^{\text{expt}}$ resembled appeared roughly +-shaped, but were X-shaped at $-\Omega_{1,2}^{\text{expt}}$. Observation of these resonance states is consistent with the models of combined potential and magnetic

scattering of quasiparticles in d -wave superconductors [19]. However, as in the case of Zn, spatial patterns deviate from the predictions [19]. In one attempt to reconcile theory and experiment a “filter” hypothesis was proposed [8]. Here, we show that the experimental features are easily obtained in the BdG+W approach and, like the Zn problem [12], tunneling via nearest-neighbor apical oxygen atoms plays a crucial role in shaping the spatial patterns at resonance energies in the local density of states (LDOS) spectrum near Ni impurities.

For the same problem in NaCCOC, we find that the Wannier functions on the surface that couple to the STM tip and the electronic structure at low energies are very similar to BSCCO despite the fact that the material has a different structure and the tunneling takes place through a rather different surface layer. Consequently, the spectral properties and the spatial pattern observed close to strong potential scatterers and also magnetic scatterers are expected to be very similar to those seen in BSCCO several Angstrom above the surface. We discuss the implications for observation of charge order in both materials, and for the use of STM to deduce important aspects of superconductivity in the cuprates.

II. MODEL

The method used in this paper was introduced earlier [11] and already applied to the case of cuprate superconductors [12] as well as in multiband systems [11,20]. The starting point is a first-principles calculation that yields the electronic structure down-folded to a tight-binding model

$$H_{\text{TB}} = Z \sum_{\mathbf{R}, \mathbf{R}'} t_{\mathbf{R}, \mathbf{R}'}^{\mu\nu} c_{\mathbf{R}\mu\sigma}^\dagger c_{\mathbf{R}'\nu\sigma} - \mu_0 \sum_{\mathbf{R}\sigma} c_{\mathbf{R}\mu\sigma}^\dagger c_{\mathbf{R}\mu\sigma}, \quad (1)$$

where $t_{\mathbf{R}, \mathbf{R}'}^{\mu\nu}$ are hopping elements between orbitals μ and ν on the lattice sites labeled with \mathbf{R} and \mathbf{R}' and $c_{\mathbf{R}\sigma}^\dagger$ creates an electron at lattice site \mathbf{R} with spin $\sigma = \pm$. To account for correlations, we introduce an overall band renormalization Z and work away from half-filling using a rigid band shift by choosing the chemical potential μ_0 accordingly. While this is a standard procedure and also a common starting point for model-based calculations, we obtain extra information with the Wannier functions that describe the electrons. The field operators of the electrons are related to the lattice operators via

$$\psi_\sigma(\mathbf{r}) = \sum_{\mathbf{R}\mu} c_{\mathbf{R}\mu\sigma} w_{\mathbf{R}\mu}(\mathbf{r}), \quad (2)$$

where the Wannier functions $w_{\mathbf{R}\mu}(\mathbf{r})$ are the matrix elements. For application of this approach to cuprates, we restrict consideration to a single Cu orbital, $\mu = \nu = d_{x^2-y^2}$.

In the following we study STM imaging of magnetic impurity states such as Ni in cuprates. A magnetic impurity acts as the source of potential as well as magnetic scattering, and can be simply modeled by the following Hamiltonian:

$$H_{\text{imp}} = \sum_{\mathbf{R}\sigma} (U_{\mathbf{R}\cdot\mathbf{R}} c_{\mathbf{R}\sigma}^\dagger c_{\mathbf{R}\sigma} + \text{H.c.}) + \sum_{\mathbf{R}\sigma} (\sigma J_{\mathbf{R}\cdot\mathbf{R}} c_{\mathbf{R}\sigma}^\dagger c_{\mathbf{R}\sigma} + \text{H.c.}) \quad (3)$$

The first term in the above Hamiltonian accounts for the potential scattering at the impurity site \mathbf{R}^* and $U_{\mathbf{R}\cdot\mathbf{R}}$ is the

impurity potential, which can be written as $U_0\delta_{\mathbf{R},\mathbf{R}'}$, where δ represents the Kronecker delta function, for a completely local impurity model. The second term in the above Hamiltonian accounts for the magnetic scattering due to the exchange interaction between the impurity magnetic moment, approximated as a classical spin, and the conduction electrons. $J_{\mathbf{R},\mathbf{R}'}$ denotes the extended exchange coupling, which can be expressed as $J_0\delta_{\mathbf{R},\mathbf{R}'}$ for the special case of completely local exchange interaction. Finally, to account for superconductivity we include a mean-field BCS term

$$H_{\text{BCS}} = \sum_{\mathbf{R},\mathbf{R}'} (\Delta_{\mathbf{R},\mathbf{R}'} c_{\mathbf{R}\uparrow}^\dagger c_{\mathbf{R}'\downarrow}^\dagger + \text{H.c.}), \quad (4)$$

where $\Delta_{\mathbf{R},\mathbf{R}'}$ are the pairing mean fields.

III. THEORETICAL APPROACH

A. T -matrix approach

For this purpose, we Fourier transform the superconducting order parameter of the homogeneous system to obtain $\Delta(\mathbf{k})$. In this paper, we assume a standard d -wave order parameter $\Delta(\mathbf{k}) = \Delta_0/2[\cos(k_x) - \cos(k_y)]$, and write down the Nambu Hamiltonian

$$H_{\text{N}}(\mathbf{k}) = \begin{pmatrix} H(\mathbf{k}) & \Delta(\mathbf{k}) \\ \Delta(\mathbf{k})^\dagger & -H(-\mathbf{k})^T \end{pmatrix}, \quad (5)$$

where the Fourier transform $H(\mathbf{k})$ of the hopping elements has been introduced. Defining a Green's function of the noninteracting electronic structure via

$$G_{\mathbf{k}}^0(\omega) = [\omega - H_{\text{N}}(\mathbf{k}) + i0^+]^{-1}, \quad (6)$$

we transform to real space

$$G_{\mathbf{R},\mathbf{R}'}^0(\omega) = \sum_{\mathbf{k}} e^{-i\mathbf{k}\cdot(\mathbf{R}-\mathbf{R}')} G_{\mathbf{k}}^0(\omega) = G_{\mathbf{R}-\mathbf{R}'}^0(\omega), \quad (7)$$

in order to calculate the Green's function in the presence of the impurity

$$G_{\mathbf{R},\mathbf{R}'}(\omega) = G_{\mathbf{R}-\mathbf{R}'}^0(\omega) + G_{\mathbf{R}}^0(\omega)T(\omega)G_{-\mathbf{R}'}^0(\omega), \quad (8)$$

using the (on-site) T matrix

$$T(\omega) = [1 - V_{\text{N,imp}}G^0(\omega)]^{-1}V_{\text{N,imp}}. \quad (9)$$

Here $G^0(\omega) = \sum_{\mathbf{k}} G_{\mathbf{k}}^0(\omega)$ is the local (on-site) Green's function, which we calculate by Fourier transform; it is just the $\mathbf{R} = \mathbf{R}'$ component of Eq. (7). The impurity potential, split up in a potential part and a magnetic contribution, is given by $V_{\text{N,imp}} = \sigma_z \otimes U_0 + 1_2 \otimes J_0$. The steps presented up to now are straightforward and widely used in the literature [4]; alternative methods to obtain the lattice Green's function $G_{\mathbf{R},\mathbf{R}'}(\omega)$ including the modulation of the order parameter in real space (via self-consistency approaches) will be presented in the next section. For the results presented in Sec. IV, we employ the T -matrix approach only for the computationally expensive calculations of STM topographs and related maps.

B. BdG approach

The mean-field solution of our problem including all terms of the Hamiltonian

$$H = H_{\text{TB}} + H_{\text{BCS}} + H_{\text{imp}} \quad (10)$$

can be found by solving a self-consistency equation where the superconducting order parameter $\Delta_{\mathbf{R},\mathbf{R}'}$ is related to the pair potential $\Gamma_{\mathbf{R},\mathbf{R}'}$ through $\Delta_{\mathbf{R},\mathbf{R}'} = \Gamma_{\mathbf{R},\mathbf{R}'} \langle c_{\mathbf{R}'\downarrow} c_{\mathbf{R}\uparrow} \rangle$. To get the d -wave gap symmetry we set $\Gamma_{\mathbf{R},\mathbf{R}'} = \Gamma$ if sites (\mathbf{R},\mathbf{R}') are nearest neighbors and 0 otherwise. The eigenvalue problem corresponding to Eq. (10) can be expressed in the form of BdG equations, which are solved self-consistently [11] for $\Delta_{\mathbf{R},\mathbf{R}'}$ and μ_0 by keeping the electron number fixed. Note that the self-consistent solution in the homogeneous case yields an order parameter with NN components only, which can be transformed to momentum space to fix the prefactor in $\Delta(\mathbf{k}) = \Delta_0/2[\cos(k_x) - \cos(k_y)]$ for the T -matrix calculation as stated above. Using BdG eigenvalues $E_{n\sigma}$ and eigenvectors $u_{n\sigma}$ and $v_{n\sigma}$, the lattice Green's function $G_{\mathbf{R}\mathbf{R}'\sigma}(\omega)$ from the self-consistent approach can be obtained as well.

C. Calculation of the tunneling conductance

The differential tunneling conductance as measured in an STM experiment at a given bias voltage V can be calculated using [21]

$$\frac{dI}{dV}(\mathbf{r}, \text{eV}) = \frac{4\pi e}{\hbar} \rho_t(0) |M|^2 \rho(\mathbf{r}, \text{eV}), \quad (11)$$

where $\rho_t(0)$ is the density of states of the tip material and $|M|^2$ is a tip-dependent tunneling matrix element. In this paper, we do not attempt to calculate these quantities, but instead analyze the properties of the differential conductance in terms of the continuum LDOS

$$\rho(\mathbf{r}, \omega) \equiv -\frac{2}{\pi} \text{Im} G^{11}(\mathbf{r}, \mathbf{r}; \omega), \quad (12)$$

where G^{11} refers to the particle-hole component of the Nambu Green's function; for broken SU(2) symmetry in spin space, one needs to take into account also the G^{22} component at negative energies

$$\rho(\mathbf{r}, \omega) \equiv -\frac{1}{\pi} [\text{Im} G^{11}(\mathbf{r}, \mathbf{r}; \omega) - \text{Im} G^{22}(\mathbf{r}, \mathbf{r}; -\omega)]. \quad (13)$$

Finally, the continuum Green's function can be calculated by employing a Wannier basis transformation [11],

$$G(\mathbf{r}, \mathbf{r}'; \omega) = \sum_{\mathbf{R}, \mathbf{R}'} G_{\mathbf{R}, \mathbf{R}'}^{\mu, \nu}(\omega) w_{\mathbf{R}\mu}(\mathbf{r}) w_{\mathbf{R}'\nu}^*(\mathbf{r}'), \quad (14)$$

where relation Eq. (2) has been used. Note that the framework can be applied to single and multiband systems, while in the following, all orbital indices are ignored since a one-band model for cuprates is used.

IV. RESULTS

A. Electronic structure

The first step in the Wannier-function-based analysis of STM observables is to construct the tight-binding description of the normal state of the material under study, using first-principles calculations. As input for the density functional theory (DFT) calculations, a cell representing the $\text{Bi}_2\text{Sr}_2\text{CaCu}_2\text{O}_8$ surface was constructed as follows. First, the bulk $\text{Bi}_4\text{Sr}_4\text{Ca}_2\text{Cu}_4\text{O}_{16}$ unit cell was considered with the structural parameters from Ref. [22]. Then half of the atoms

were deleted, resulting in a single $\text{Bi}_2\text{Sr}_2\text{CaCu}_2\text{O}_8$ layer unit cell with a vacuum of approximately 20 \AA , see Fig. 1(a). A single $\text{Ca}_2\text{CuO}_2\text{Cl}_2$ (CCOC) layer unit cell was created in a similar way. First, the bulk $\text{Ca}_4\text{CuO}_4\text{Cl}_4$ unit cell was considered with structural parameters taken from Ref. [23]. Then again half of the atoms were deleted, which creates a certain amount of vacuum. In addition, some vacuum was added such that the total vacuum is again approximately 20 \AA . The DFT calculations and subsequent down-folding to the Wannier basis, were performed using the VASP [24] and WANNIER90 [25] packages, respectively (see Appendix for details). After the construction of the tight-binding model, calculations are performed for 15% doping implemented by a rigid band shift, roughly appropriate for optimal doping.

As shown in Figs. 1(c) and 1(d), we obtain a very similar tight-binding structure for both BSCCO and CCOC, which is generic for many cuprate materials. The Wannier functions generated in this down-folding procedure involve states derived from all atomic species in the unit cell, but restricted to an energy range of a few eV around the Fermi level. The Cu $d_{x^2-y^2}$ Wannier function important for superconductivity is shown in Fig. 2 to involve not only atomic $d_{x^2-y^2}$ functions on a given site, but states localized on many nearby atoms. The tunneling process depends on the density of these states, and those associated with Wannier functions on neighboring Cu's, at a point several Å above the surface. At intermediate isovalues, i.e., distances from a given Cu, the Wannier function is seen in Fig. 2 to be rather complex, and differences between BSCCO and CCOC are evident, reflecting differences in the barrier layer. While in both cases, apical p_z states above the nearest-neighbor Cu are clearly visible, in the BSCCO case these are associated with O, while in CCOC they are associated with the Cl. There are also qualitative differences that may be observed upon close inspection of the figure.

However, in the asymptotic regime far from the surface, the Wannier functions for both materials are seen to be almost identical. The symmetry of the Cu $d_{x^2-y^2}$ wave function is the same as dictated by the symmetry of the crystal including the atoms in the layers above the Cu-O layer leading to the vanishing weight directly above the central Cu site; small differences in the extent of the wave function, e.g., the positions of the maxima relative to the center, can be observed, see Figs. 2(d) and 2(h). The maximum in the magnitude of the Wannier function in both compounds occurs above the NN Cu sites. It was shown in Ref. [12] that this maximum has the largest contribution from the apical O- p states in NN unit cells. In case of CCOC, we find that the NN Cl- p states at the surface are responsible for the Wannier function maxima. The similarity of the shape of the surface Wannier function in both compounds leads to the similar spatial structure of impurity states at the STM tip position, as we show in following sections.

B. Effects of a nonmagnetic impurity

Now, we describe the effects of a strong potential scatterer such as Zn in the superconducting state of NaCCOC, and compare it with BSCCO. We use an on-site impurity potential of $U_0 = -5 \text{ eV}$ to model Zn-like potential scatterer. A very similar value to the impurity potential was obtained from the

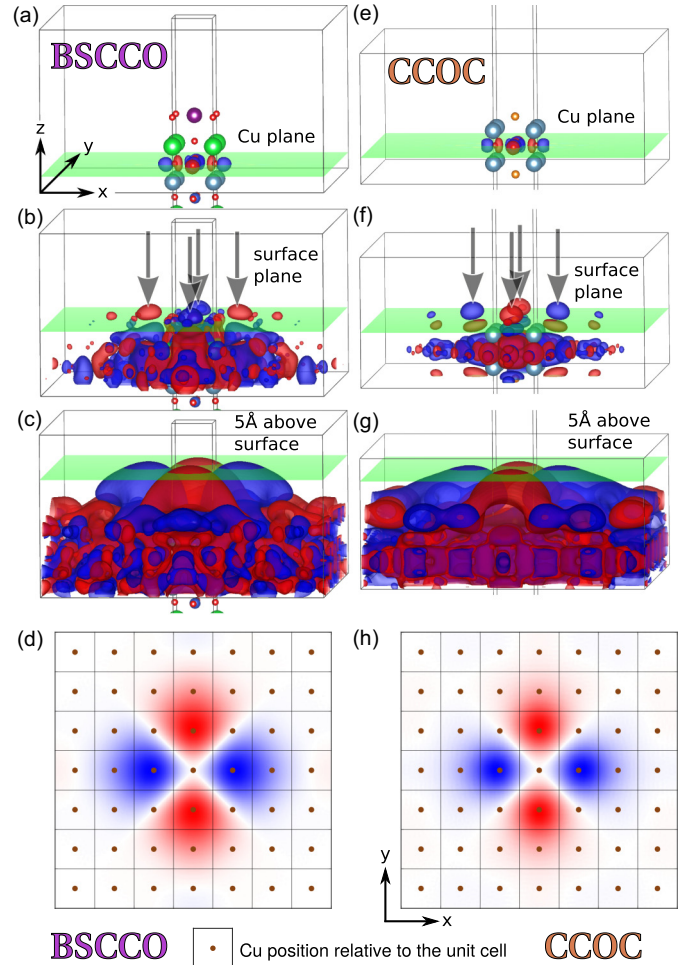


FIG. 2. Wannier function of (a)–(d) $\text{Bi}_2\text{Sr}_2\text{CaCu}_2\text{O}_8$ and (e)–(h) $\text{Ca}_2\text{CuO}_2\text{Cl}_2$ plotted at three different isovalues and as a color map approximately 5 \AA above the surface exposed to the STM tip, as used for the simulations of STM conductance maps and spectra. The green planes in the isosurface plots lie in the plane of the Cu atoms, the plane of the surface atoms and 5 \AA above the surface atoms, respectively. The lobes of the Wannier function originating from hybridization with orbitals of the surface atoms are indicated by arrows in (b), (f). These correspond to apical O and apical Cl p_z states in (b) and (f), respectively. The isovalues in $\text{bohr}^{-3/2}$ are the following: 5×10^{-2} (a), (e); 5×10^{-4} (b); 5×10^{-3} (f); 5×10^{-5} (c); 3×10^{-5} (g). The coordinate system used throughout this paper is indicated as inset in (a).

first-principles calculations for Zn substituting a Cu atom in BSCCO [12]. The effects of correlations are crudely accounted for by scaling down all hopping parameters by a mass renormalization factor $1/Z = 3(2.3)$ for BSCCO (NaCCOC) so that the Fermi velocities match with the corresponding experimental values [26,27]. Note that STM experiments probing Zn and Ni impurity induced states in BSCCO [6,18] were performed in the optimal-to-overdoped regime where effects of strong correlation are less important; such a mass renormalization is therefore a reasonable way to incorporate correlations. The d -wave superconductivity is introduced by hand through a pairing interaction on NN bonds with pair potential $\Gamma = 0.17(0.15) \text{ eV}$ for BSCCO (NaCCOC), such

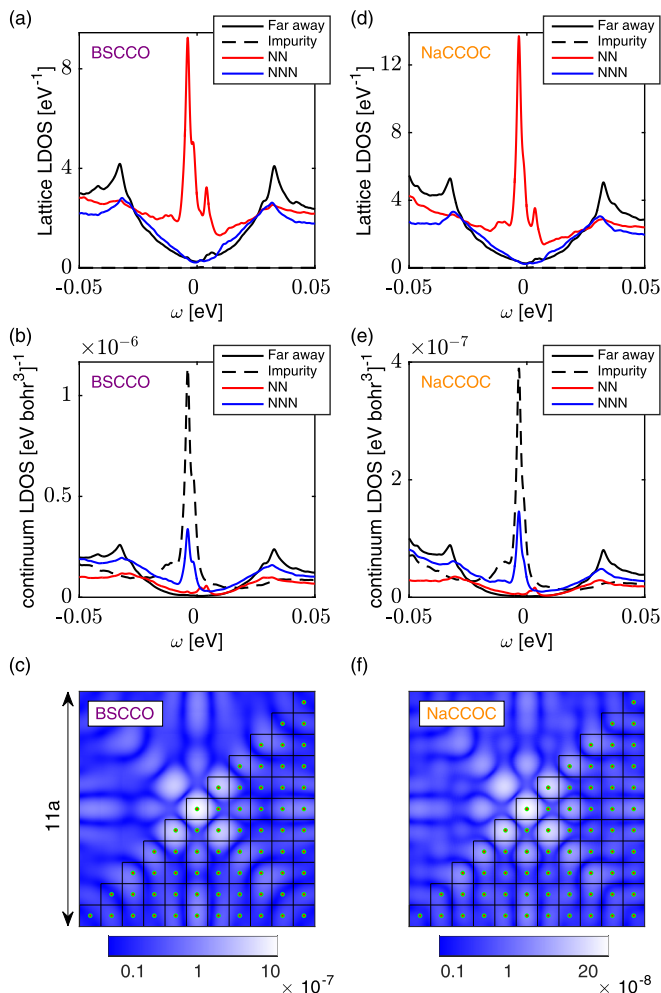


FIG. 3. (a) Lattice LDOS spectrum around a strong, nonmagnetic, Zn-like impurity, replacing Cu in BSCCO, with on-site potential $U_0 = -5$ eV. Spectrum at a site far from the impurity (black), impurity site (dashed), nearest-neighbor site (red), and next-nearest-neighbor site (blue) is calculated using 30×30 supercells with artificial broadening of 1 meV. (b) Continuum LDOS spectrum at a height approximately 5 \AA above the BiO surface. Shown are positions directly above a Cu atom far from impurity (black), at the impurity (dashed), on the nearest-neighbor position (red), and on the next-nearest-neighbor position (blue). (c) Continuum LDOS map in the vicinity of impurity obtained at the resonance energy $\Omega = -4$ meV and a height approximately 5 \AA above the BiO surface. Color bar values are in the units of $\text{eV}^{-1} \text{bohr}^{-3}$. Small black squares denote CuO_2 unit cells, with Cu positions marked by red-green circles. (d)–(f) Same quantities as in (a)–(c), respectively, for the impurity replacing Cu in NaCCOC. The LDOS map in (e) is obtained at the resonance energy $\Omega = -3.4$ meV.

that a d -wave gap with $\Delta(\mathbf{k}) = \Delta_0/2[\cos(k_x) - \cos(k_y)]$, with $\Delta_0 \approx 33$ meV is obtained for both BSCCO and NaCCOC. Note that the coherence peak positions and therefore the gap maxima are less clear in the tunneling spectra for NaCCOC than for BSCCO; we set the Δ_0 's equal only to highlight the other materials-specific differences between the systems that we study here. Figures 3(a) and 3(d) show the lattice LDOS in the vicinity of a Zn-like impurity in BSCCO and NaCCOC, respectively. A sharp bound state at $\pm\Omega = 4(3.4)$ meV is

observed in the BSCCO (NaCCOC) lattice LDOS spectrum at the NN site, whereas the lattice LDOS at the impurity site is completely suppressed, as one would expect from a strong impurity. As pointed out in Ref. [12] and illustrated in Figs. 3(b) and 3(c), the experimentally observed [6] spatial distribution of spectra in Zn-doped BSCCO is recovered in the continuum LDOS, obtained at a height $\approx 5 \text{ \AA}$ above the BiO surface using Eq. (12), which shows a sharp peak at $\omega = -\Omega$ directly above the impurity site, and large intensity at the NNN sites in the spatial map at this resonance energy. More importantly for the focus of this paper, the impurity-induced states in NaCCOC should follow the same pattern, as illustrated in Figs. 3(e) and 3(f). This is due to the fact that the Wannier function cut at heights a few Å above the surface (BiO layer in BSCCO and Cl layer in NaCCOC) in both materials are qualitatively very similar, in spite of different surface atoms. While to our knowledge there are no experiments on Zn impurities in NaCCOC, the BdG+W calculations predict that Zn in that system should give rise to the same patterns of impurity-induced states as in BSCCO.

The qualitative difference between lattice LDOS and continuum LDOS is not only visible in the vicinity of the impurity, but also at sites far from the impurity where a more U-shaped spectrum [see Figs. 3(b) and 3(e)] than seen in the usual V-shaped lattice LDOS [see Figs. 3(a) and 3(d)] is found. This unusual U-shaped behavior is actually observed in various STM experiments on the overdoped cuprates [28–32]. As discussed in detail in the Appendix, this change of low-energy spectrum can be attributed to the particular form of the Wannier function, which vanishes directly above the central Cu site (d -wave symmetry) and attains its largest value at the NN sites, see Figs. 2(d) and 2(h). A simple calculation (see Appendix) shows that the low-energy continuum LDOS spectrum above a Cu site, at heights a few Å above the surface, varies as $\rho(\mathbf{r}, \omega \rightarrow 0) \sim |\omega|^3$ yielding a more U-shaped structure. The suppression of the linear- ω term can be traced back to the occurrence of nonlocal contributions to the continuum Green's function [13]. It is interesting to speculate why STM data seems to indicate a crossover from U-shaped (overdoped) to V-shaped (underdoped), possibly related to the variation of the range of the Wannier function as correlations grow [33], but we have not arrived at a completely satisfactory description of this effect. In any case, the current calculations are applicable only to the more weakly correlated (overdoped) regime.

So far, we have discussed the calculation of the differential conductance following Eq. (11) by evaluating the continuum LDOS at fixed height above the surface. Experimentally, the differential conductance maps are usually taken in topographic mode, i.e., while scanning the STM tip over an area by keeping the current I_0 at a given bias voltage V_0 constant such that the height $z(x, y)$ varies with the position (x, y) [6,18,34,35]. Theoretically, we can simulate a topograph by solving the equation [11]

$$I_0 = \frac{4\pi e}{\hbar} \rho_t(0) |M|^2 \int_0^{eV_0} d\omega \rho(x, y, z(x, y), \omega), \quad (15)$$

for the height map $z(x, y)$ for given I_0 and V_0 . Indeed, this requires the calculation of the continuum LDOS within a height range and for all energies to carry out the integral.

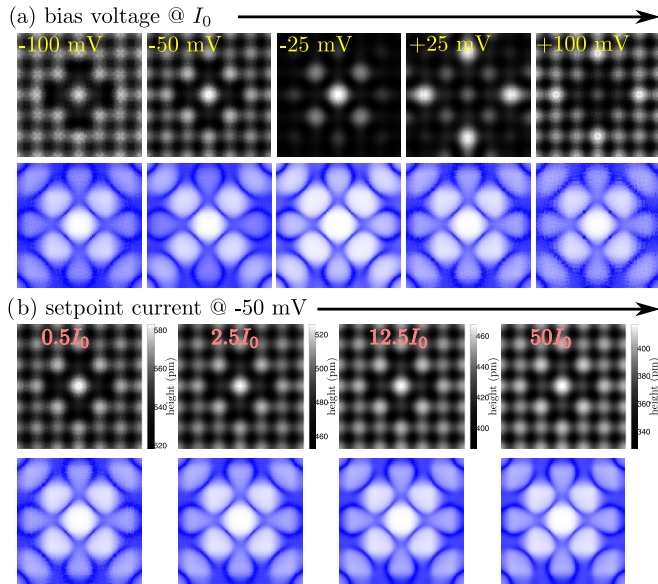


FIG. 4. Simulation of bias and set-point current dependence on topographies for NaCCOC (black and white) and topographic conductance maps (blue white, logarithmic scale) at the resonance energy $\Omega = -2.5$ meV: (a) Changing the bias voltage from negative to positive changes the shape of the impurity in the topography (top row), but has little influence on the corresponding topographic conductance map at the resonance energy (bottom row). (b) Changing the set-point current for the topography does change the overall height, but has almost no influence on the shape as seen in the topography and the topographic conductance maps.

Since we find little difference in the results between the BdG approach and a T -matrix calculation for the relevant quantities (see Appendix), these calculations have been done with the less computationally expensive T -matrix approach only, as outlined in Sec. III A. For the strong potential scatterer $U_0 = -5$ eV, the calculation of topographs has been carried out for NaCCOC only, with the result as presented in Fig. 4 where in the top rows black and white topographic maps are shown for a fixed current I_0 but with varying set-point voltage V_0 [Fig. 4(a)] and for a fixed set-point voltage V_0 with varying current I_0 over several orders of magnitude [Fig. 4(b)]. Indeed, the topographs change with the set-point bias V_0 , since the integral in Eq. (15) is dominated by the real-space structure of the impurity resonance at negative energies for $V_0 = -25$ mV and at positive energies for $V_0 = +25$ mV while at large bias voltage (positive or negative) a larger part of the tunneling current I_0 comes from electronic states that are dominated by normal state features. The topographs for fixed current bias voltage V_0 but varying current I_0 [as shown in Fig. 4(b)], are very similar except that the overall height is moved down when increasing the current. This is a property of the continuum LDOS and consequently the simulated tunneling conductance being in the exponential limit [12]. With the simulated height map $z(x, y)$ in hand, we can also simulate topographic conductance maps $G(x, y, eV)$ as measured in experiment by using $G(x, y, eV) \propto \rho(x, y, z(x, y), eV)$. For each topograph in Fig. 4, we also show the topographic conductance maps $G(x, y, \Omega)$ at the resonance energy Ω , with the result that differences are visible in the relative height of the features

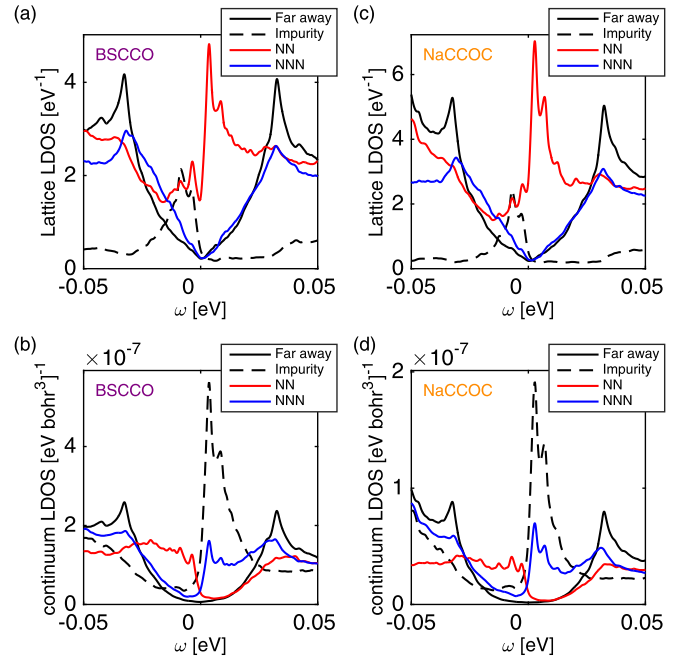


FIG. 5. (a) Lattice LDOS spectrum around a magnetic impurity, replacing Cu in BSCCO, with on-site potential $U_0 = 0.6$ eV and on-site exchange coupling $J_0 = 0.3U_0$. Spectrum at a site far from the impurity (black), impurity site (dashed), nearest-neighbor site (red), and next-nearest-neighbor site (blue) is calculated using 30×30 supercells with artificial broadening of 1 meV. (b) Continuum LDOS spectrum at a height approximately 5 \AA above the BiO surface. Shown are positions directly above a Cu atom far from impurity (black), at the impurity (dashed), on the nearest neighbor position (red), and on the next-nearest-neighbor position (blue). (c), (d) same quantities as in (a) and (b), respectively, for the same magnetic impurity replacing Cu in NaCCOC.

at the positions above the NN, NNN, and NNNN Cu atoms, a consequence of the STM tip being closer to the surface or further away depending on the choice of the set-point voltage V_0 .

C. Effects of a magnetic impurity

We now study magnetic impurity-induced states induced by Ni in BSCCO and NaCCOC. Theoretical results on both materials show very similar behavior due to similar tight-binding parameters and Wannier functions. Ni is known to be a weaker impurity than Zn as it does not disrupt superconductivity in its vicinity, and the pure magnetic scattering is thought to be subdominant to the pure potential scattering [18]. In the absence of magnetic scattering, the resonance peaks are spin degenerate. A small on-site exchange coupling J_0 lifts this degeneracy as the effective impurity potential experienced by the electrons becomes spin dependent $V_{\text{imp}}^{\text{eff}} = U_0 + \sigma J_0$, and leads to two spin polarized in-gap resonance states.

Accordingly, in the simplest scenario, we model Ni as a completely local impurity, with on-site potential $U_0 = 0.6$ eV and exchange coupling $J_0 = 0.3U_0$, placed in the center of a 35×35 lattice. Figures 5(a) and 5(c) show the lattice LDOS spectrum at different sites around such an impurity in BSCCO and NaCCOC, respectively. For BSCCO (NaCCOC),

impurity-induced resonance peaks at $\pm\Omega_1 = 3.6(2.7)$ meV and $\pm\Omega_2 = 8.6(7)$ meV are easily observed in the LDOS spectrum at the impurity site and its NN. Resonance peaks at $+\Omega_1$ and $-\Omega_2$ have down-spin polarization whereas those at $+\Omega_2$ and $-\Omega_1$ have up-spin polarization. By contrast, the spectrum at the NNN site simply follows the bulk LDOS spectrum. The particular values of U_0 and J_0 have been chosen just to clearly demonstrate the spin-splitting of impurity-induced resonance peaks due to on-site magnetic scattering. The experimentally observed sharp resonance peaks close to the gap edge [18] can not be reproduced in this simple model, due to significant broadening of peaks close to the gap edge [4].

In order to directly compare with the STM conductance [18], we must calculate the continuum LDOS at a typical STM tip position. Figures 5(b) and 5(d) show the continuum LDOS spectrum in BSCCO and NaCCOC, respectively, at $z \approx 5$ Å above the surface at positions that are directly above the impurity, NN site, NNN site, and a distant site. In both materials, similar to the STM result [18], the continuum LDOS exhibits a double peak structure at negative (positive) energies at the positions directly above NN site (impurity and NN sites). Note that this trend is completely missing in the lattice LDOS spectrum [Figs. 5(a) and 5(c)].

Now we turn to the spatial LDOS maps at the resonance energies in BSCCO. Figure 6(a) shows the lattice LDOS map at $\omega = +\Omega_1$ around impurity in a region comprising 11×11 unit cells. The vanishing LDOS at the impurity site and maximum at the NN site observed here is completely opposite to the experimental conductance map at $\omega = +\Omega_1^{\text{expt}}$ reproduced in Fig. 6(c). However, the continuum LDOS map $\rho(\mathbf{r}, +\Omega_1)$, at a height ≈ 5 Å above the BiO plane, shown in Fig. 6(b) compares very well with the experiment. A similar trend holds at the negative energy resonance peak. The continuum LDOS map at $\omega = -\Omega_1$ shown in Fig. 6(e) shows excellent agreement with the experimental conductance map at $\omega = -\Omega_1^{\text{expt}}$ reproduced in Fig. 6(f). The continuum LDOS map at $\omega = +\Omega_2$ ($-\Omega_2$) is found to be very similar to that at $\omega = +\Omega_1$ ($-\Omega_1$).

Finally, we note that even though the simple on-site magnetic impurity model captures the spin-splitting of impurity resonance peaks and yields correct spatial patterns of LDOS, a careful comparison with the STM conductance spectrum shows that the relative peak heights are reversed compared to experiment. The experimentally observed relative peak heights can not be explained by an on-site magnetic impurity model as the height of the resonance peak decreases and width increases as it moves away from the midgap due to increasing hybridization between bulk and impurity states [4]. In the Appendix, we show that an extended impurity model can yield the experimentally observed relative peak heights, and retain the same continuum LDOS patterns.

V. CONCLUSIONS

In this paper, we have tackled the longstanding question of why STM on cuprate surfaces is apparently universal, despite the fact that chemically quite different barrier layers tend to separate the CuO_2 plane from the STM tip above the surface. Using a recently developed Wannier-based treatment of the local electronic structure combined with d -wave supercon-

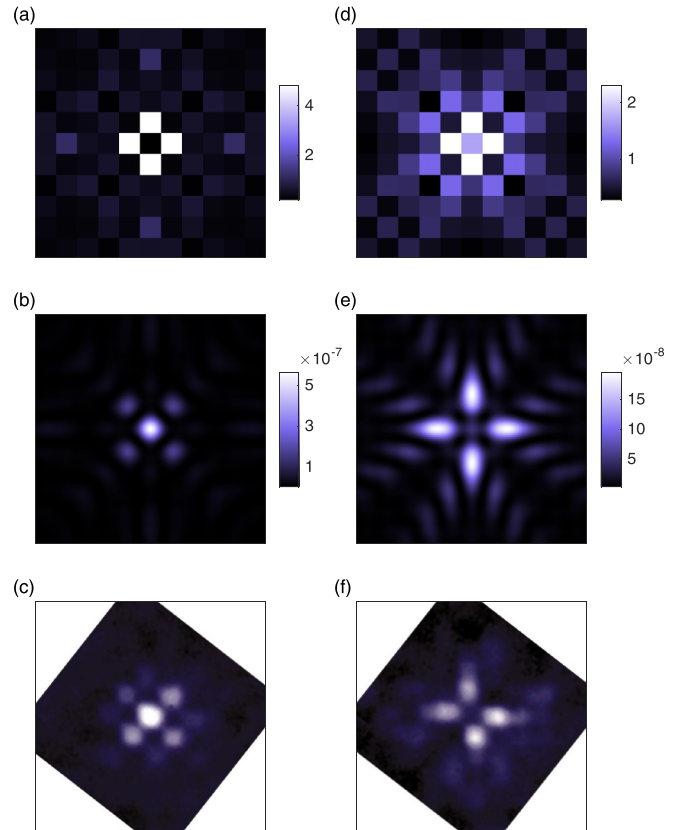


FIG. 6. (a), (d) Lattice LDOS map around a magnetic impurity in BSCCO in a region comprising 11×11 unit cells at the resonant energies $\Omega_1 = 3.6$ and -3.6 meV, respectively. Color bar values are in the units of eV^{-1} . (b), (e) Continuum LDOS maps at $\Omega_1 = 3.6$ and -3.6 meV, respectively, and approximately 5 Å above BiO plane with same area as in (a) and (d). Color bar values are in the units of $\text{eV}^{-1} \text{bohr}^{-3}$. (c), (f) STM conductance maps at $\Omega_1^{\text{expt}} = 9$ meV and -9 meV, respectively, reproduced from Ref. [18], rotated to match the orientation in (b) and (e), and cropped to 11×11 elementary cells with the Ni impurity located at the center.

ductivity, we provided a simple explanation of this universality based on the simple form of the Cu $d_{x^2-y^2}$ Wannier function several Å above the surface at the tip position. We showed that while these functions are completely different in the vicinity of the CuO_2 plane and inside the barrier layer for two cuprate systems commonly used in STM, BSCCO and NaCCOC, their tails detected by the STM tip are remarkably similar. This fact alone should lead to the nearly identical charge order patterns observed in both materials [17], provided, of course, that the charge ordered states in the CuO_2 plane are in fact the same.

To illustrate the effect of this filtered tunneling process and how it affects the spatial conductance patterns observed, we presented again some details of the conductance maps and topographs for a Zn impurity in BSCCO, shown earlier [12] to provide a remarkably good agreement with the Zn conductance maps observed in STM over many years. As expected from the above discussion, similar calculations for NaCCOC reproduce extremely similar patterns. This represents a prediction for future experiments, since to our knowledge no experiments on Zn in NaCCOC have been performed. In addition, we studied

the Ni impurity problem in BSCCO with the Wannier-based method, obtaining for the BSCCO system conductance maps with extremely good agreement with experimental maps at the resonance energies. Very similar results were obtained for NaCCOC. Some small discrepancies with the height of the two resonances relative to experiment in BSCCO were noted, and discussed in terms of the range of the Ni impurity potential. Similar calculations were presented for NaCCOC, again with similar patterns predicted.

We have furthermore pointed out an interesting problem regarding the low-energy tunneling conductance that has been noted before phenomenologically [36] but not analyzed microscopically. The d -wave form of the Wannier function at the tip position strongly suppresses the linear- ω bias dependence of the continuum LDOS, leading to a predicted U-shaped characteristic. Indeed, data on overdoped cuprates appears to show this behavior, while for underdoped samples a V-shaped spectrum is observed. We discussed possible effects that might explain the crossover from U- to V-shaped spectra in terms of enhanced correlations in the underdoped phase.

The situation with charge order in the two materials is considerably more subtle, and may depend on a deeper understanding of the origins of charge order in both materials. Recent comparison of inhomogeneous stripelike charge states of the t - J model, dressed with Wannier functions using the current method [13], suggest that these are indeed of universal origin, and appear identical in the two systems because of the simple form of the Wannier functions above the plane. Future analysis of STM data on this important problem in cuprate physics should use the Wannier-based method to ensure accurate conclusions regarding correlations in the CuO_2 plane itself.

ACKNOWLEDGMENTS

The authors wish to acknowledge useful discussions with J. C. Davis, A. Kostin, W. Ku, and P. Sprau. P.C. and P.J.H. were supported by Grant No. NSF-DMR-1407502. P.C. acknowledges the research grant PDF/2017/002242 from SERB, DST, India. B.M.A. acknowledges support from Lundbeckfond fellowship (Grant No. A9318). Work by T.B. was performed at the Center for Nanophase Materials Sciences, a DOE Office of Science user facility. This research used resources of the National Energy Research Scientific Computing Center, a DOE Office of Science User Facility supported by the Office of Science of the US DOE under Contract No. DE-AC02-05CH11231.

APPENDIX

1. Homogeneous state continuum LDOS

Transforming to the momentum-space basis, Eqs. (13) and (14) lead to the following expression for the continuum LDOS in a homogeneous system.

$$\rho_\sigma(\mathbf{r}, \omega) = \sum_{\mathbf{k}} A_\sigma(\mathbf{k}, \omega) |W_{\mathbf{k}}(\mathbf{r})|^2. \quad (\text{A1})$$

Here, $W_{\mathbf{k}}(\mathbf{r}) = \sum_{\mathbf{R}} w_{\mathbf{R}}(\mathbf{r}) e^{i\mathbf{k}\cdot\mathbf{R}}$ is the Fourier transform of the Wannier function, and $A_\sigma(\mathbf{k}, \omega)$ is the spectral function, which

can be written as

$$A_\sigma(\mathbf{k}, \omega) = |u_{\mathbf{k}}|^2 \delta(\omega - E_{\mathbf{k}}) + |v_{\mathbf{k}}|^2 \delta(\omega + E_{\mathbf{k}}), \quad (\text{A2})$$

where $E_{\mathbf{k}} = \sqrt{\xi_{\mathbf{k}}^2 + \Delta_{\mathbf{k}}^2}$, with $\xi_{\mathbf{k}}$ the band energy relative to the Fermi level, $\Delta_{\mathbf{k}} = \Delta_0(\cos k_x - \cos k_y)$ the superconducting gap, and $|u_{\mathbf{k}}|^2 = \frac{1}{2}(1 + \frac{\xi_{\mathbf{k}}}{E_{\mathbf{k}}}) = 1 - |v_{\mathbf{k}}|^2$ the coherence factors.

For the continuum position above the Cu site, $\mathbf{r}_0 = [0, 0, z]$, at heights z several Å above the BiO plane, the dominant contribution to $W_{\mathbf{k}}(\mathbf{r})$ comes from the Wannier function at the nearest-neighbor sites (see Fig. 2). Accordingly

$$W_{\mathbf{k}}(\mathbf{r}_0) \approx w_0 + 2w_1(\cos k_x - \cos k_y), \quad (\text{A3})$$

where, w_0 and w_1 are the values of the Wannier function at $\mathbf{r} = \mathbf{r}_0$, and $\mathbf{r} = \mathbf{r}_0 + a\hat{x}$, where a is the in-plane lattice constant. The $d_{x^2-y^2}$ -wave symmetry of the Wannier function dictates that $w_0 = 0$, however, we still keep it to facilitate discussions in following paragraphs. The higher harmonics neglected in Eq. (A3) will not qualitatively change our final conclusions regarding the shape of the continuum LDOS spectrum at low energies.

Using Eqs. (A1)–(A3), we can express the continuum LDOS above a Cu site for $\omega > 0$ as

$$\begin{aligned} \rho_\sigma(\mathbf{r}_0, \omega) &= \rho^{00} + \rho^{10} + \rho^{11} \\ \rho^{00} &= \frac{1}{2} w_0^2 \sum_{\mathbf{k}} \left(1 + \frac{\xi_{\mathbf{k}}}{E_{\mathbf{k}}}\right) \delta(\omega - E_{\mathbf{k}}) \\ \rho^{10} &= 2w_0 w_1 \sum_{\mathbf{k}} \left(1 + \frac{\xi_{\mathbf{k}}}{E_{\mathbf{k}}}\right) (\cos k_x - \cos k_y) \delta(\omega - E_{\mathbf{k}}) \\ \rho^{11} &= 2w_1^2 \sum_{\mathbf{k}} \left(1 + \frac{\xi_{\mathbf{k}}}{E_{\mathbf{k}}}\right) (\cos k_x - \cos k_y)^2 \delta(\omega - E_{\mathbf{k}}). \end{aligned} \quad (\text{A4})$$

For $\omega \rightarrow 0$, the dominant contributions to the above integrals will be from the nodal regions of the Brillouin zone. Accordingly, we shift the origin to the nodal point $\mathbf{k}_0 = [k_x^0, k_y^0]$, with $k_x^0 = k_y^0 = \frac{1}{\sqrt{2}} k_0$, and rotate the coordinate axes to k_1 and k_2 as shown in Fig. 7. Linearizing the band dispersion and gap, we get $\xi_{\mathbf{k}} \approx v_F k_2$ and $\Delta_{\mathbf{k}} \approx v_\Delta k_1$ where v_F is the Fermi velocity at node and $v_\Delta = \sqrt{2} \Delta_0 \sin k_x^0$. With these simplifications, ρ^{00} in Eq. (A4) becomes

$$\begin{aligned} \rho^{00} &= \frac{1}{2} M w_0^2 \iint_{\Omega} \frac{d\mathbf{k}}{(2\pi)^2} \left(1 + \frac{v_F k_2}{\sqrt{v_\Delta^2 k_1^2 + v_F^2 k_2^2}}\right) \\ &\times \delta(\omega - \sqrt{v_\Delta^2 k_1^2 + v_F^2 k_2^2}), \end{aligned} \quad (\text{A5})$$

where Ω is a circular region around the nodal point \mathbf{k}_0 with radius Γ , and $M = 4$ is the number of nodes. The above integral can be simplified by scaling the coordinates as $k'_1 = v_\Delta k_1$ and $k'_2 = v_F k_2$, followed by a transformation to the polar coordinates with $k'_1 = k' \cos \theta'$ and $k'_2 = k' \sin \theta'$,

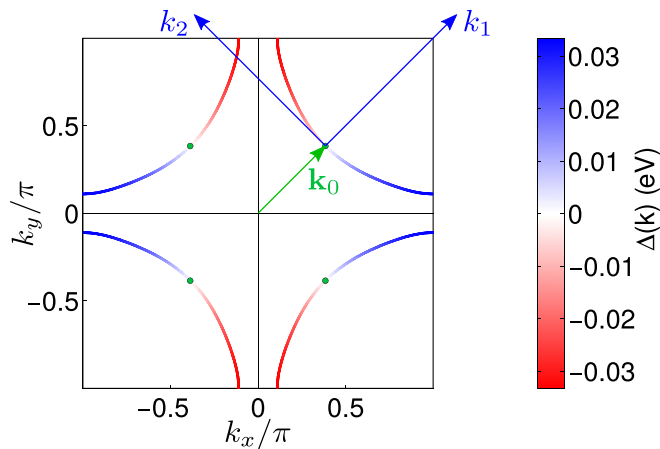


FIG. 7. The d -wave order parameter has $M = 4$ nodes (green dots) at the Fermi surface, which is shown as an example for BSCCO. The coordinate system (k_1, k_2) with axes parallel and perpendicular to a nodal direction (blue arrows) and origin located at the node \mathbf{k}_0 in the first quadrant (green arrow) is also shown.

resulting into

$$\begin{aligned} \rho^{00} &= \frac{1}{(2\pi)^2} \frac{M w_0^2}{2v_F v_\Delta} \int_0^\Gamma \int_0^{2\pi} k' dk' d\theta' (1 + \sin \theta') \delta(\omega - k') \\ &= \left(\frac{w_0^2}{\pi v_F v_\Delta} \right) \omega. \end{aligned} \quad (\text{A6})$$

Proceeding in a similar manner, we can evaluate ρ^{11} as

$$\begin{aligned} \rho^{11} &= 2w_1^2 M \iint_{\Omega} \frac{d\mathbf{k}}{(2\pi)^2} \left(1 + \frac{v_F k_2}{\sqrt{v_\Delta^2 k_1^2 + v_F^2 k_2^2}} \right) \\ &\quad \times (2\sqrt{2}t k_1 \sin k_x^0)^2 \delta(\omega - \sqrt{v_\Delta^2 k_1^2 + v_F^2 k_2^2}) \\ &= \frac{4M w_1^2 \sin^2 k_x^0}{(2\pi)^2 v_F v_\Delta^3} \int_0^\Gamma \int_0^{2\pi} k' dk' d\theta' \delta(\omega - k') \\ &\quad \times (k'^2 \cos^2 \theta' + \sin \theta' \cos^2 \theta') \\ &= \left(\frac{4w_1^2 \sin^2 k_x^0}{\pi^3 v_F v_\Delta^3} \right) \omega^3. \end{aligned} \quad (\text{A7})$$

Finally, ρ^{10} turns out to be zero due to vanishing angular integrals. Thus,

$$\begin{aligned} \rho_\sigma(\mathbf{r}_0, \omega) &= a_0 \omega + a_1 \omega^3, \\ a_0 &= \frac{w_0^2}{\pi v_F v_\Delta}, \\ a_1 &= \frac{4w_1^2 \sin^2 k_x^0}{\pi^3 v_F v_\Delta^3}. \end{aligned} \quad (\text{A8})$$

The coefficient of the linear in ω term vanishes as $w_0 = 0$ due to $d_{x^2-y^2}$ symmetry of the Wannier function; however, the coefficient of the ω^3 term is nonzero, and yields a U-shaped spectrum at low energies. The equivalent result was obtained earlier using a purely phenomenological model for the hopping between cuprate layers [36]. Setting $W_{\mathbf{k}}(\mathbf{r}) = 1$ in Eq. (A1) [or equivalently $w_0 = 1, w_1 = 0$ in Eq. (A3)] yields

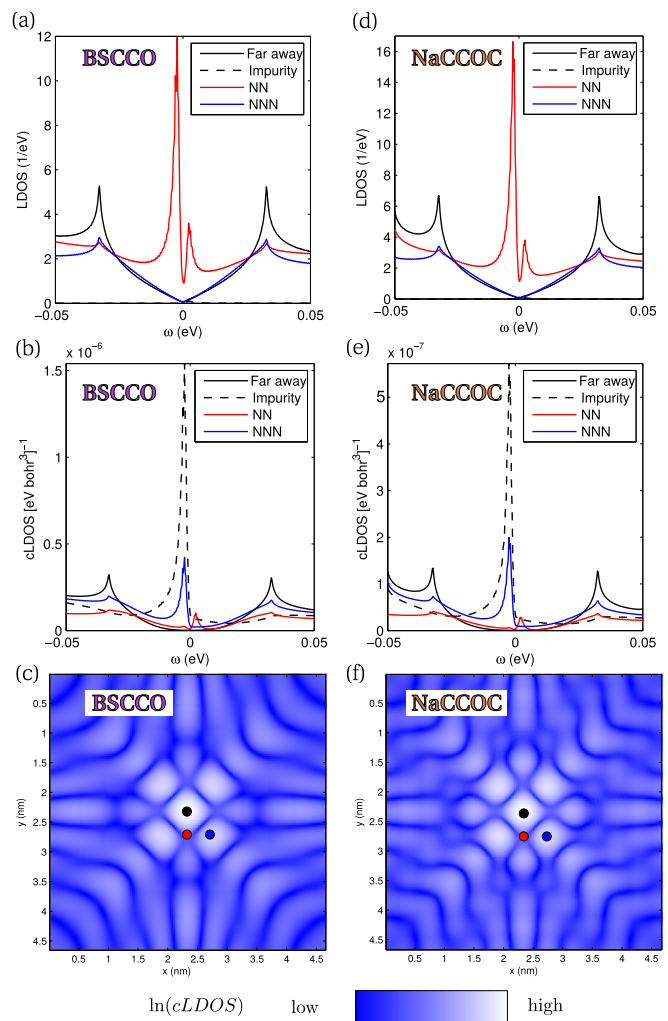


FIG. 8. Results for a strong potential scatterer $U_0 = -5$ eV using the T -matrix formalism with 2500×2500 k points and a smearing of $\eta = 0.25$ meV. As in Fig. 3, the lattice LDOS, the continuum LDOS (cLDOS) spectrum, and cLDOS map at a height ≈ 5 Å above the surface for the resonance energy is plotted both for BSCCO and NaCCOC.

the lattice LDOS $N(\omega)$, which, from Eq. (A8), turns out to vary linearly with ω , leading to the well-known V-shaped spectrum at low energies.

2. Details of continuum LDOS spectrum in the vicinity of an impurity

As argued already in the main text, the results for various quantities in presence of an impurity do not significantly depend on whether the T -matrix formalism or the self-consistent BdG method is used. The latter is indeed numerically more demanding because self-consistency in the densities and the superconducting order parameter is required and diagonalization of large matrices is needed. To show explicitly the correspondence of the results, we present in Fig. 8 the same quantities as plotted in Fig. 3, but calculated within the T -matrix formalism. Keeping this in mind, we can safely look at T -matrix results only for the continuum LDOS spectra in the vicinity of a strong impurity. The different shape

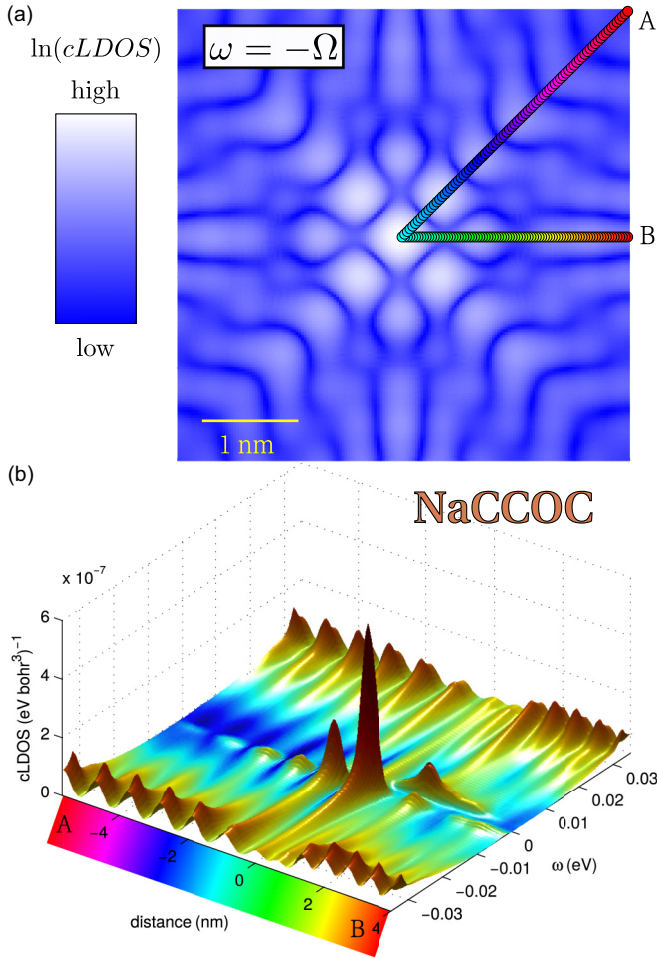


FIG. 9. Spatial evolution of the spectra close to a strong impurity in NaCCOC: (a) continuum LDOS (cLDOS) map from a T -matrix calculation, plotted on an area of 12×12 elementary cells, at the resonance energy $\omega = -\Omega$. Spectra are then plotted in (b) along the path shown in (a), from point A to the impurity position and then along the Cu-Cu bond direction to point B. The strong impurity resonance peak at the impurity position is visible, along with further peaks at $\omega = -\Omega$ along the diagonal and oscillating peaks at $\omega = +\Omega$ and $\omega = -\Omega$ along the Cu-Cu bond direction.

of the impurity pattern in the continuum LDOS at resonance is also reflected in the spectra taken at different points in real space. For example, if one plots the spectrum along a path away from the impurity, one sees that along the diagonals of the continuum LDOS maps at positive resonance energy Ω , no intensity can be seen, while along the Cu-Cu bond direction, the conductance shows a periodic variation. The situation is different for the conductance at negative resonance energy $-\Omega$, where strong variations are seen at the diagonals, and weak variations are seen along the Cu-Cu bonds direction. The same behavior is also demonstrated in Fig. 9 where such a path along the diagonal to the impurity and then along the Cu-Cu bond direction away from the impurity is defined in Fig. 9(a). The spectra along this path as shown in Fig. 9(b) then exhibit periodic modulations of the $-\Omega$ peak along the diagonal and alternating (decreasing) peaks at $+\Omega$ and $-\Omega$

when moving away from the impurity along the Cu-Cu bond direction toward point B.

3. Normalized conductance maps

In the main text, we discussed that differential conductance maps slightly depend on the experimental conditions at which the tunneling junction is set up to scan along the surface. A possible way to eliminate this dependence on the experimental parameters (I_0 and V_0) is to consider the normalized conductance [35]

$$K(x, y, eV) = V \frac{\frac{dI}{dV}(x, y, eV)}{I(x, y, eV)}, \quad (\text{A9})$$

which is the ratio of the measured differential conductance and the (at the same time) registered current $I(x, y, eV)$, normalized by the voltage V . As pointed out in Ref. [35], this quantity is also independent of whether the data has been taken at constant height conditions or constant current conditions (topographic mode) and should be examined in linear scale instead of logarithmic as the conductance maps.

Following our approach for the calculation of differential conductance and current, Eqs. (11) and (15), we can theoretically obtain this quantity

$$\begin{aligned} K(x, y, eV) &= V \frac{\rho(x, y, z(x, y), eV)}{\int_0^{eV} d\omega \rho(x, y, z(x, y), \omega)} \\ &= V \frac{\rho_p(x, y, eV)}{\int_0^{eV} d\omega \rho_p(x, y, \omega)}. \end{aligned} \quad (\text{A10})$$

In the exponential limit, the continuum LDOS will have an exponential dependence on the height $\rho(x, y, z(x, y)) \approx e^{-\alpha z(x, y)} \rho_p(x, y)$ that dropped out from the formula (A10) with the last equal sign, such that it is not necessary to calculate the topographic map $z(x, y)$. For quantities that are particle-hole symmetric, a similar removal of the set-point effect can be achieved in two ways: A division of the conductance by the conductance at negative bias yields the quantity

$$Z(x, y, eV) = \frac{\frac{dI}{dV}(x, y, eV)}{\frac{dI}{dV}(x, y, -eV)}. \quad (\text{A11})$$

Finally, one can also divide the current at positive bias by the current at negative bias to get

$$R(x, y, eV) = \frac{I(x, y, eV)}{I(x, y, -eV)}, \quad (\text{A12})$$

which shows similar features. An example of such an R map around a strong $U_0 = -5$ eV impurity is shown in Fig. 10. The Z map is extremely similar.

4. Extended magnetic impurity model

Although the splitting of peaks due to magnetic scattering is captured in the simple model of a pointlike impurity as discussed in Sec. IV C, a careful comparison with the experimental conductance spectrum shows that the relative heights of the peaks are reversed. In the simple on-site impurity model, the height of the resonance peak decreases and width increases as it moves away from the midgap due to increasing hybridization between bulk and impurity states [4]. Thus

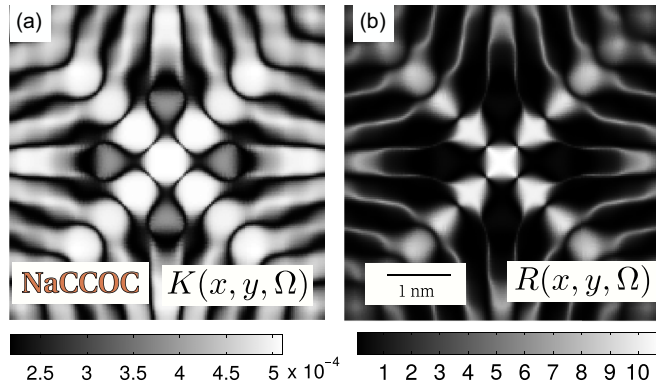


FIG. 10. (a) Calculated K map of a strong impurity and (b) R map of the same impurity in NaCCOC. The energy is fixed to the resonance energy Ω and the size of the field of view is 12 unit cells.

the experimentally observed relative peak heights can not be explained by such model. To this end, we find that an extended impurity model with on-site potential $U_0 = 0.6$ eV, NN potential $U_{NN} = 0.3$ eV, and NN exchange coupling $J_{NN} = U_{NN}$ can lead to the desired trend [37,38]. This impurity model yields sharp resonance peaks at $\pm\Omega_1 = 4.2$ meV and $\pm\Omega_2 = 18.6$ meV in the lattice and continuum LDOS spectrum as shown in Figs. 11(a) and 11(b), respectively. Clearly, resonance peaks at $\pm\Omega_2$ are higher than those at $\pm\Omega_1$. Moreover, similar to the experiment and also to the case of on-site impurity model, continuum LDOS shown in Fig. 11(b) displays switching of resonance peaks from positive to negative biases and then back to positive biases as one moves from impurity to NN and then to NNN sites. Thus, the extended impurity model captures most of the features of STM results [18]; however, the microscopic origin of such a model still needs to be investigated.

5. Details of first-principles calculations

The DFT calculations were performed within the generalized gradient approximation (GGA) using the Perdew-Burke-Ernzerhof exchange correlation scheme and projector augmented wave potentials [39] as implemented in VASP [24,40]. We used a $7 \times 7 \times 1$ k -point grid and a relatively high kinetic energy cutoff of 2000 eV to ensure high-quality Wannier functions. To capture the Wannier functions we

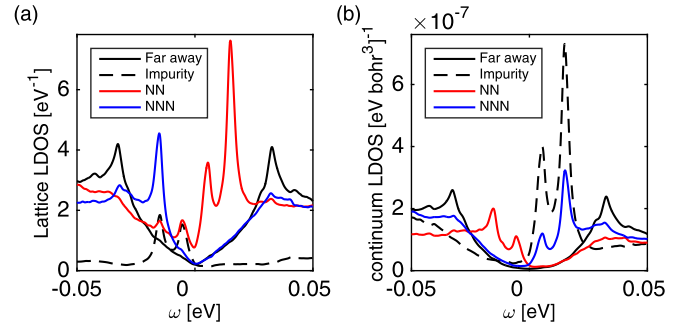


FIG. 11. (a) Lattice LDOS spectrum around a magnetic impurity, replacing Cu in BSCCO, with on-site potential $U_0 = 0.6$ eV, NN potential $U_{NN} = 0.5U_0$, and NN exchange coupling $J_{NN} = 0.5U_0$. Spectrum at a site far from the impurity (black), impurity site (dashed), nearest-neighbor site (red), and next-nearest-neighbor site (blue) is calculated using 30×30 supercells with artificial broadening of 1 meV. (b) Continuum LDOS spectrum at a height ≈ 5 Å above the BiO surface. Shown are positions directly above a Cu atom far from impurity (black), at the impurity (dashed), on the nearest-neighbor position (red), and on the next-nearest-neighbor position (blue).

projected the Cu- $d_{x^2-y^2}$ orbital on the bands within $[-3, 3]$ eV. DFT bands close to the Fermi level have dominant Cu- $d_{x^2-y^2}$ character, making it an appropriate choice for projection to study superconductivity, a low-energy phenomenon, within a one-band tight-binding model. Given that a Wannier transformation is essentially a basis transformation, the proper hybridization with other atomic states, to the extent already captured within DFT, is ensured. We used WANNIER90 [25] in which we set num_iter=0 to retain the correct symmetry of the $d_{x^2-y^2}$ orbital and dis_num_iter = 1000. For the $\text{Ca}_2\text{CuO}_2\text{Cl}_2$ Wannier calculation we set dis_froz_min = -0.9 and dis_froz_max = 2.5 to better capture the bands near the Fermi energy. To reduce the two-band Wannier function based Hamiltonian of $\text{Bi}_2\text{Sr}_2\text{CaCu}_2\text{O}_8$ to a single-band Hamiltonian we simply cut the (relatively weak) hopping elements that couple two Cu planes. Atomic and three-dimensional Wannier function images were produced with the VESTA program [41]. Finally, we note that the features of the BSCCO Cu- $d_{x^2-y^2}$ Wannier function obtained here are almost identical to that reported in Ref. [12], even though a different DFT package and projection scheme have been used.

- [1] Ø. Fischer, M. Kugler, I. Maggio-Aprile, C. Berthod, and C. Renner, Scanning tunneling spectroscopy of high-temperature superconductors, *Rev. Mod. Phys.* **79**, 353 (2007).
- [2] K. Fujita, A. R. Schmidt, E.-A. Kim, M. J. Lawler, D. H. Lee, J. C. Davis, H. Eisaki, and S. Uchida, Spectroscopic imaging scanning tunneling microscopy studies of electronic structure in the superconducting and pseudogap phases of cuprate high-Tc superconductors, *J. Phys. Soc. Jpn.* **81**, 011005 (2012).
- [3] J. Nieminen, I. Suominen, R. S. Markiewicz, H. Lin, and A. Bansil, Spectral decomposition and matrix element effects in

scanning tunneling spectroscopy of $\text{Bi}_2\text{Sr}_2\text{CaCu}_2\text{O}_{8+\delta}$, *Phys. Rev. B* **80**, 134509 (2009).

- [4] A. V. Balatsky, I. Vekhter, and J.-X. Zhu, Impurity-induced states in conventional and unconventional superconductors, *Rev. Mod. Phys.* **78**, 373 (2006).
- [5] H. Alloul, J. Bobroff, M. Gabay, and P. J. Hirschfeld, Defects in correlated metals and superconductors, *Rev. Mod. Phys.* **81**, 45 (2009).
- [6] S. H. Pan, E. W. Hudson, K. M. Lang, H. Eisaki, S. Uchida, and J. C. Davis, Imaging the effects of individual zinc impurity atoms

- on superconductivity in $\text{Bi}_2\text{Sr}_2\text{CaCu}_2\text{O}_{8+\delta}$, *Nature (London)* **403**, 746 (2000).
- [7] A. V. Balatsky, M. I. Salkola, and A. Rosengren, Impurity-induced virtual bound states in d -wave superconductors, *Phys. Rev. B* **51**, 15547 (1995).
- [8] I. Martin, A. V. Balatsky, and J. Zaanen, Impurity States and Interlayer Tunneling in High Temperature Superconductors, *Phys. Rev. Lett.* **88**, 097003 (2002).
- [9] J.-X. Zhu, C. S. Ting, and C.-R. Hu, Effect of unitary impurities on non-STM types of tunneling in high- T_c superconductors, *Phys. Rev. B* **62**, 6027 (2000).
- [10] L.-L. Wang, P. J. Hirschfeld, and H.-P. Cheng, Ab initio calculation of impurity effects in copper oxide materials, *Phys. Rev. B* **72**, 224516 (2005).
- [11] P. Choubey, T. Berlijn, A. Kreisel, C. Cao, and P. J. Hirschfeld, Visualization of atomic-scale phenomena in superconductors: Application to FeSe, *Phys. Rev. B* **90**, 134520 (2014).
- [12] A. Kreisel, P. Choubey, T. Berlijn, W. Ku, B. M. Andersen, and P. J. Hirschfeld, Interpretation of Scanning Tunneling Quasiparticle Interference and Impurity States in Cuprates, *Phys. Rev. Lett.* **114**, 217002 (2015).
- [13] P. Choubey, W.-L. Tu, T.-K. Lee, and P. J. Hirschfeld, Incommensurate charge ordered states in the t - t' - J model, *New J. Phys.* **19**, 013028 (2017).
- [14] K. Fujita, C. K. Kim, I. Lee, J. Lee, M. H. Hamidian, I. A. Firmo, S. Mukhopadhyay, H. Eisaki, S. Uchida, M. J. Lawler, E.-A. Kim, and J. C. Davis, Simultaneous transitions in cuprate momentum-space topology and electronic symmetry breaking, *Science* **344**, 612 (2014).
- [15] R. Comin and A. Damascelli, Resonant x-ray scattering studies of charge order in cuprates, *Annu. Rev. Condens. Matter Phys.* **7**, 369 (2016).
- [16] M. H. Hamidian, S. D. Edkins, C. K. Kim, J. C. Davis, A. P. Mackenzie, H. Eisaki, S. Uchida, M. J. Lawler, E.-A. Kim, S. Sachdev, and K. Fujita, Atomic-scale electronic structure of the cuprate d -symmetry form factor density wave state, *Nature Phys.* **12**, 150 (2016).
- [17] Y. Kohsaka, C. Taylor, K. Fujita, A. Schmidt, C. Lupien, T. Hanaguri, M. Azuma, M. Takano, H. Eisaki, H. Takagi, S. Uchida, and J. C. Davis, An intrinsic bond-centered electronic glass with unidirectional domains in underdoped cuprates, *Science* **315**, 1380 (2007).
- [18] E. W. Hudson, K. M. Lang, V. Madhavan, S. H. Pan, H. Eisaki, S. Uchida, and J. C. Davis, Interplay of magnetism and high- T_c superconductivity at individual Ni impurity atoms in $\text{Bi}_2\text{Sr}_2\text{CaCu}_2\text{O}_{8+\delta}$, *Nature (London)* **411**, 920 (2001).
- [19] M. I. Salkola, A. V. Balatsky, and J. R. Schrieffer, Spectral properties of quasiparticle excitations induced by magnetic moments in superconductors, *Phys. Rev. B* **55**, 12648 (1997).
- [20] S. Chi, R. Aluru, U. R. Singh, R. Liang, W. N. Hardy, D. A. Bonn, A. Kreisel, B. M. Andersen, R. Nelson, T. Berlijn, W. Ku, P. J. Hirschfeld, and P. Wahl, Impact of iron-site defects on superconductivity in LiFeAs, *Phys. Rev. B* **94**, 134515 (2016).
- [21] J. Tersoff and D. R. Hamann, Theory of the scanning tunneling microscope, *Phys. Rev. B* **31**, 805 (1985).
- [22] M. S. Hybertsen and L. F. Mattheiss, Electronic Band Structure of $\text{CaBi}_2\text{Sr}_2\text{Cu}_2\text{O}_8$, *Phys. Rev. Lett.* **60**, 1661 (1988).
- [23] D. N. Argyriou, J. D. Jorgensen, R. L. Hitterman, Z. Hiroi, N. Kobayashi, and M. Takano, Structure and superconductivity without apical oxygens in $(\text{Ca},\text{Na})_2\text{CuO}_2\text{Cl}_2$, *Phys. Rev. B* **51**, 8434 (1995).
- [24] G. Kresse and J. Furthmüller, Efficient iterative schemes for ab initio total-energy calculations using a plane-wave basis set, *Phys. Rev. B* **54**, 11169 (1996).
- [25] A. A. Mostofi, J. R. Yates, G. Pizzi, Y.-S. Lee, I. Souza, D. Vanderbilt, and N. Marzari, An updated version of wannier90: A tool for obtaining maximally-localised wannier functions, *Comput. Phys. Commun.* **185**, 2309 (2014).
- [26] A. Damascelli, Z. Hussain, and Z.-X. Shen, Angle-resolved photoemission studies of the cuprate superconductors, *Rev. Mod. Phys.* **75**, 473 (2003).
- [27] X. J. Zhou, T. Yoshida, A. Lanzara, P. V. Bogdanov, S. A. Kellar, K. M. Shen, W. L. Yang, F. Ronning, T. Sasagawa, T. Kakeshita, T. Noda, H. Eisaki, S. Uchida, C. T. Lin, F. Zhou, J. W. Xiong, W. X. Ti, Z. X. Zhao, A. Fujimori, Z. Hussain, and Z.-X. Shen, High-temperature superconductors: Universal nodal Fermi velocity, *Nature (London)* **423**, 398 (2003).
- [28] S. H. Pan, J. P. O'Neal, R. L. Badzey, C. Chamon, H. Ding, J. R. Engelbrecht, Z. Wang, H. Eisaki, S. Uchida, A. K. Gupta, K.-W. Ng, E. W. Hudson, K. M. Lang, and J. C. Davis, Microscopic electronic inhomogeneity in the high- T_c superconductor $\text{Bi}_2\text{Sr}_2\text{CaCu}_2\text{O}_{8+x}$, *Nature (London)* **413**, 282 (2001).
- [29] Y. Kohsaka, C. Taylor, P. Wahl, A. Schmidt, J. Lee, K. Fujita, J. W. Alldredge, K. McElroy, Jinho Lee, H. Eisaki, S. Uchida, D.-H. Lee, and J. C. Davis, How cooper pairs vanish approaching the mott insulator in $\text{Bi}_2\text{Sr}_2\text{CaCu}_2\text{O}_{8+\delta}$, *Nature (London)* **454**, 1072 (2008).
- [30] K. McElroy, D.-H. Lee, J. E. Hoffman, K. M. Lang, J. Lee, E. W. Hudson, H. Eisaki, S. Uchida, and J. C. Davis, Coincidence of Checkerboard Charge Order and Antinodal State Decoherence in Strongly Underdoped Superconducting $\text{Bi}_2\text{Sr}_2\text{CaCu}_2\text{O}_{8+\delta}$, *Phys. Rev. Lett.* **94**, 197005 (2005).
- [31] J. W. Alldredge, J. Lee, K. McElroy, M. Wang, K. Fujita, Y. Kohsaka, C. Taylor, H. Eisaki, S. Uchida, P. J. Hirschfeld, and J. C. Davis, Evolution of the electronic excitation spectrum with strongly diminishing hole density in superconducting $\text{Bi}_2\text{Sr}_2\text{CaCu}_2\text{O}_{8+\delta}$, *Nature Phys.* **4**, 319 (2008).
- [32] K. M. Lang, V. Madhavan, J. E. Hoffman, E. W. Hudson, H. Eisaki, S. Uchida, and J. C. Davis, Imaging the granular structure of high- T_c superconductivity in underdoped $\text{Bi}_2\text{Sr}_2\text{CaCu}_2\text{O}_{8+\delta}$, *Nature (London)* **415**, 412 (2002).
- [33] A. P. Kkardzielawa, J. Spátek, J. Kurzyk, and W. Wójcik, Extended Hubbard model with renormalized Wannier wave functions in the correlated state III, *Eur. Phys. J. B* **86**, 252 (2013).
- [34] T. Hanaguri, Y. Kohsaka, J. C. Davis, C. Lupien, I. Yamada, M. Azuma, M. Takano, K. Ohishi, M. Ono, and H. Takagi, Quasiparticle interference and superconducting gap in $\text{Ca}_{2-x}\text{Na}_x\text{CuO}_2\text{Cl}_2$, *Nature Phys.* **3**, 865 (2007).
- [35] R. M. Feenstra, Tunneling spectroscopy of the (110) surface of direct-gap III-V semiconductors, *Phys. Rev. B* **50**, 4561 (1994).
- [36] Y. H. Su, H. G. Luo, and T. Xiang, Universal scaling behavior of the c -axis resistivity of high-temperature superconductors, *Phys. Rev. B* **73**, 134510 (2006).
- [37] J.-M. Tang and M. E. Flatté, Van hove features in $\text{Bi}_2\text{Sr}_2\text{CaCu}_2\text{O}_{8+\delta}$ and effective parameters for Ni impurities inferred from STM spectra, *Phys. Rev. B* **66**, 060504 (2002).

- [38] A. Polkovnikov, S. Sachdev, and M. Vojta, Impurity in a d -Wave Superconductor: Kondo Effect and STM Spectra, *Phys. Rev. Lett.* **86**, 296 (2001).
- [39] P. E. Blöchl, Projector augmented-wave method, *Phys. Rev. B* **50**, 17953 (1994).
- [40] G. Kresse and D. Joubert, From ultrasoft pseudopotentials to the projector augmented-wave method, *Phys. Rev. B* **59**, 1758 (1999).
- [41] K. Momma and F. Izumi, VESTA3 for three-dimensional visualization of crystal, volumetric and morphology data, *J. Appl. Cryst.* **44**, 1272 (2011).